Journal of Alloys and Compounds 822 (2020) 153609

Contents lists available at ScienceDirect

Journal of Alloys and Compounds

journal homepage: http://www.elsevier.com/locate/jalcom

Hot workability of Co–Fe–Mn–Ni–Ti eutectic high entropy alloy

Reliance Jain [a], M R Rahul [b], Sumanta Samal [a, *], Vinod Kumar [a], Gandham Phanikumar [b]

[a] *Discipline of Metallurgy Engineering and Materials Science, Indian Institute of Technology Indore, Khandwa Road, Simrol, Indore, 453552, Madhya Pradesh, India*

[b] *Department of Metallurgical and Materials Engineering, Indian Institute of Technology Madras, Chennai, 600036, Tamil Nadu, India*

ARTICLE INFO

Article history:
Received 1 September 2019
Received in revised form
18 December 2019
Accepted 30 December 2019
Available online 31 December 2019

Keywords:
Eutectic high entropy alloy
SEM
XRD
Processing maps
Finite element simulation

ABSTRACT

Multicomponent $Co_{25}Fe_{25}Mn_5Ni_{25}Ti_{20}$ eutectic high entropy alloy (EHEA), synthesized by vacuum arc melting followed by suction casting method resulted in two types of solid solution phases (fcc CoFeNi-rich (α) and bcc Ti-rich (β)) and $Ti_2(Ni, Co)$ type Laves phase. The hot deformation behaviours have been investigated at a temperature ranging from 1073 to 1273 K and different strain rates (10^{-3},10^{-2},$10^{-1}$and 1 s^{-1}). The optimum hot workability conditions of EHEA lies in temperature range 1073–1273 K and strain rate range 10^{-3} s^{-1}-$10^{-1.6}$ s^{-1} as well as temperature 1130–1225K and strain rate $10^{-0.5}$-1 s^{-1}. The constitutive relation is established to understand the plastic deformability at high temperature. Finite element simulation has also been used to predict the deformation behaviour during the hot working process.

1. Introduction

Recently, multicomponent high entropy alloys (HEAs) have attracted increasing attention because of their unique microstructures with different composition and excellent mechanical properties. HEAs are composed of five or more than five major elements in equal or nearly equal atomic percent (at. %) and/or some other minor elements [1]. Generally, Eutectic HEAs (EHEAs) are described as solid solution phase with other secondary phases to obtain good mechanical properties [2–6]. EHEAs show superior properties such as high strength and ductility, creep resistance, good microstructural stability at high temperature, possess excellent mechanical properties, have good castability and hence can be considered as potential candidates for high-temperature applications [7]. The mechanical properties of EHEAs are attributed to Hall-Petch mechanism. In multicomponent EHEAs, the characteristic length-scale is observed to be very small and the strength is high due to refinement of eutectic lamellae [8]. Hall-Patch equation for eutectic alloys is defined as $\sigma_{ye} = \sigma_{ie} + K\ \lambda_e^{-1/2}$ where the σ_{ye} is the yield strength of the material, σ_{ie} is the friction stress, λ_e is the inter-lamellar spacing of the eutectic microstructure and K is the hall patch slope [8].

In the case of single-phase HEAs, there is a problem associated with the balancing of strength and ductility. Further, single-phase HEAs with fcc structure, good ductility is obtained but not adequate strength whereas single-phase bcc HEA materials show good strength and low ductility [9–12]. Thus to solve this problem, researchers are now working in the way of designing composite HEAs to achieve an optimum combination of strength and ductility. The processing of metals and alloys are always accompanied by a different hot working process such as rolling, forging and extrusion. Therefore, it is of great significance to investigate the hot deformation behaviour of high entropy alloys under hot processing conditions. The activation energy value is used mainly to find the predominant mechanism during hot deformation [13–15]. Hence, several reports have been devoted so far to calculate activation energy for the hot deformation of different alloys. Because activation energy depends on the resistance to plastic deformation, which is estimated by using different flow equation, involving the response of flow stress, deformation temperature and strain rate [16]. It is reported in the literature [14] that the addition of minor elements such as Nb, V and Ti in the commercial alloys increases the activation energy. In the present study, the non-equiatomic EHEA is designed to contain Ti as one of the elements and the increase in the activation energy of the system is perhaps expected and hence can be used for thermomechanical processing of materials at high temperature. Reyes-Calderón et al. [16] also found that the activation energy of the different multicomponent alloy

---

* Corresponding author.
E-mail address: sumanta@iiti.ac.in (S. Samal).

https://doi.org/10.1016/j.jallcom.2019.153609

systems which is controlled by the mechanism of dynamic recovery (DRV) and dynamic recrystallisation (DRX).

In the current study, The hot deformation behaviour and processing map of $Co_{25}Fe_{25}Mn_{5}Ni_{25}Ti_{20}$ EHEA were motivated by the previous study on Phase evolution and mechanical behaviour of Co–Fe–Mn–Ni–Ti eutectic high entropy alloys [17]. The objective is to identify the optimum thermomechanical processing (TMP) condition of EHEA by generating the contour plots using different parameters as well as to determine the activation energy through kinetics analysis. Further, the finite element method (FEM) simulation has been carried out based on the experimental conditions to identify the plastic strain variation within the sample.

1.1. *Experimental details*

High purity elemental forms of Co, Fe, Mn, Ni, and Ti (purity level $\geq$ 99.7) were used as starting material. The non-equiatomic $Co_{25}Fe_{25}Mn_{5}Ni_{25}Ti_{20}$ alloy ingot is prepared by vacuum arc melting cum suction castings method under argon gas (with ultra-high purity level 99.999%) in the water-cooled copper hearth plate. For melting, TIG torch with non-consumable W-electrode was used. The material ingot is melted 5–6 times to attain the chemical homogeneity. Bruker D2 phaser X-ray diffractometer with CuKα ($\lambda = 1.54056$ Å) radiation, operating at 45 kV and 30 mA, with a step size of $2\theta = 0.017°$ is used for structural characterization of studied EHEA. The microstructural characterization and composition analysis of constituent phases of studied non-equiatomic EHEA were done using the scanning electron microscope (INSPECT F SEM coupled with Oxford INCA 300 X-ray energy dispersive spectrometer).

To understand the hot deformation behaviours of EHEA at high temperature and different strain rates Gleeble@3800 thermo-mechanical simulator with hydrawedge module is used to perform isothermal hot compression tests. Specimen used is rod-shaped (Ø = 6 mm and an aspect ratio of 1.5:1). The uni-axial hot compression tests were performed at the temperatures, i.e. 800 °C (1073 K), 900 °C (1173 K) and 1000 °C (1273 K) nominal strain rates of 0.001, 0.01, 0.1 and 1 s^{-1}. Graphite sheet, along with Ni paste, was used between sample ends and anvil to reduce friction during hot compression. Before compression test, all the specimens were heated at a heating rate of 5 K/s from room temperature to the desired hot-working temperature and held there for 5 min to reach homogeneous temperature distribution throughout the entire specimen. It is to be noted that all the hot compression tests were carried out under an argon atmosphere. The samples were subjected to a 50% reduction in the height and then immediately water quenched to room temperature to maintain its deformed microstructure. The flow curve (true stress-strain) information was recorded for all strain rates and deformation temperatures during the process of hot compression. Subsequently, Microstructural analysis of the deformed samples was carried out along the compression axis.

1.2. *Thermodynamics simulation*

The CALculation of PHAse Diagram (CALPHAD) approach is the foundation of materials design, and recognising the full potential of HEAs needs such computational tools to optimise alloy parameters within the complication of the HEA composition space [18]. It is a robust tool to estimate the thermodynamic properties of the multi-component system, by extrapolating the existing lower order system with efficient manner. Details of the algorithm in thermodynamic simulation:

- Firstly, extrapolate the Gibbs free energy of the existing lower order system and then for a higher-order system by using a well-established model such as Muggianu's method [19], Kohler's method [20], Toop's method [21] etc.
- Secondly, CALPHAD method considering the Gibbs energy of all phases and reduces the total Gibbs free energy of the system. For multi-component system, total Gibbs free energy of a phase given by the equation:

$$G^{\varphi} = G^{S} + G^{ideal} + G$$

Where the G^S is the standard Gibbs free energy of the mechanical mixing of constitute phases, G^{ideal} is the Gibbs free energy of mixing of ideal, G^E is the excess free energy.

- Finally, the stable phases in the multicomponent system obtained by the minimisation of total Gibbs free energy of the system i.e. $G = \sum_{i=1}^{n} [n_i G^{\Phi}]]$ [22] should be minimum, where the n_i amount of phases and G^{Φ} is Gibbs free energy.

Nowadays, for the study of HEAs well established CALPHAD based software packages such as Thermo-Calc®, FactSage® [23], Pandat® [24] are available and extensively used [25].

In the present study, the thermodynamic simulation of the studied EHEA has been carried out using ThermoCalc® software with TCHEA2® database to understand the solidification pathways. The phase formation during the solidification is generally understood by two classical solidification models such as Lever rule and Gulliver-Scheil models [26]. Lever rule model of solidification assumes the complete mixing of solutes in liquid as well as solid, which predicts the equilibrium solidification pathways. The solute balance equation in Lever rule model for equilibrium solidification can be expressed as $C_l = \frac{C_i}{1-(1-K)\,fs}$ [26]; While in Gulliver-Scheil model, the redistribution of solute during the solidification is described by considering no diffusion in solid, complete diffusion in liquid and the local equilibrium at the interface. Also, at the solid-liquid interface, the liquid concentration expressed as $C_l = C_i(1-fs)^{K-1}$ [26]; where C_i is the initial liquid concentration, K is the equilibrium partition constant and f_s is a solid fraction. Therefore, Gulliver-Scheil model is considered as a suitable model for predicting phase evolution during non-equilibrium solidification because of limited diffusion of solute in solid [27].

1.3. *FEM simulation*

The simulation of the hot deformation process was done using ABAQUS software at different deformation temperatures and strain rates conditions. By governing the loading velocity and time, the average strain rate is achieved for hot deformation. The simulation was performed using a quadrilateral element with mesh size 0.25 mm and assumed the 3D model. The meshing of the model of hot deformed EHEA cylinder was done in ABAQUS FE tool with C3D8R elements. Adaptive mesh control manager in ABAQUS/Explicit method was performed due to the substantial deformation expected during the process, maintaining the high quality of the mesh and hence reduces the chances of mesh distortion during the analysis. The mechanical properties of materials different temperature from flow curves obtained from the Gleeble®. The properties which are not available from flow curves, together with thermal properties, are calculated using the rule of mixture. The properties of EHEA such as density, Young's modulus, Poisson's ratio, thermal conductivity, shear modulus and coefficient of thermal expansion are 7.6954 gm/cm^3, 188.1 GPa, 0.225, 72.285 W/m-K, 107.755 GPa and 1.2355×10^{-5} K^{-1} respectively. The finite element simulation of a hot compression test of EHEA was carried out using an interface friction factor of 0.5 between the die and the workpiece interface. The effective plastic strain field during plastic deformation is established.

2. Result and discussion

2.1. Thermodynamic analysis by CALPHAD method

The thermodynamic simulation is done for the prediction of phases which are developed in HEAs during solidification by using ThermoCalc® software (thermo-Calc Software, salona, Sweden) with TCHEA2® database. Fig. 1(A) shows the amount of phases *Vs.* Temperature and Fig. 1(a) temperature *Vs.* mole fraction of solid, indicting the solidification pathways of $Co_{25}Fe_{25}Mn_5Ni_{25}Ti_{20}$ EHEA. It is important to note that FCC_L12, FCC_L12#2, FCC_L12#3, BCC_B2, C14_laves are observed to form directly from the liquid phase. While SIGMA, BCC_B2, Ni_3Ti_D024, C15_laves phases are formed during solid-state transformation.

2.2. Structural analysis

The XRD pattern of $Co_{25}Fe_{25}Mn_5Ni_{25}Ti_{20}$ multicomponent eutectic high entropy alloys is shown in Fig. 1(b). The XRD plot indicates the presence of BCC phase (β), FCC phase (α) and Ti_2(Co, Ni) type laves phase. It is to be noted here that all predicted equilibrium phases are not observed in studied EHEA, which is attributed to the high cooling rate achieved during the non-equilibrium solidification processing of EHEA.

2.3. Microstructural characterization

The microstructural characterization of EHEA is carried out by FESEM with backscattered electron mode (as given in Fig. 1(c)). The different phases present in studied EHEA are marked based on the elemental analysis using EDS attached with FESEM. The microstructure shows a solid solution phase having Ti-rich with black contrast (β), Fe—Co—Ni-rich with bright contrast (α) and Ti_2(Co, Ni) type Laves phase with grey contrast. It is to be noted that the Ti-rich phase (β) is bounded by Ti_2(Co, Ni) type Laves phase, signifying peritectic reaction. It is found that peritectic reaction occurs between bcc Ti-rich (β) and liquid phase to yield secondary fcc CoFeNi-rich (α) phase. While the eutectic reaction occurs between fcc CoFeNi-rich (α) phase and Ti_2(Ni, Co) type Laves phase.

3. Mechanical properties of multicomponent EHEA

3.1. Flow behaviour of hot compressed materials

During hot-compression tests, the Stress *Vs.* Strain plots at different temperature and strain rate are given in Fig. 2. Furthermore, it is observed that the stress increases with an increase in the strain rate and decreases with increase in temperature [28]. During the hot deformation, mainly two mechanisms such as strain hardening and softening plays a vital role. Before the maximum

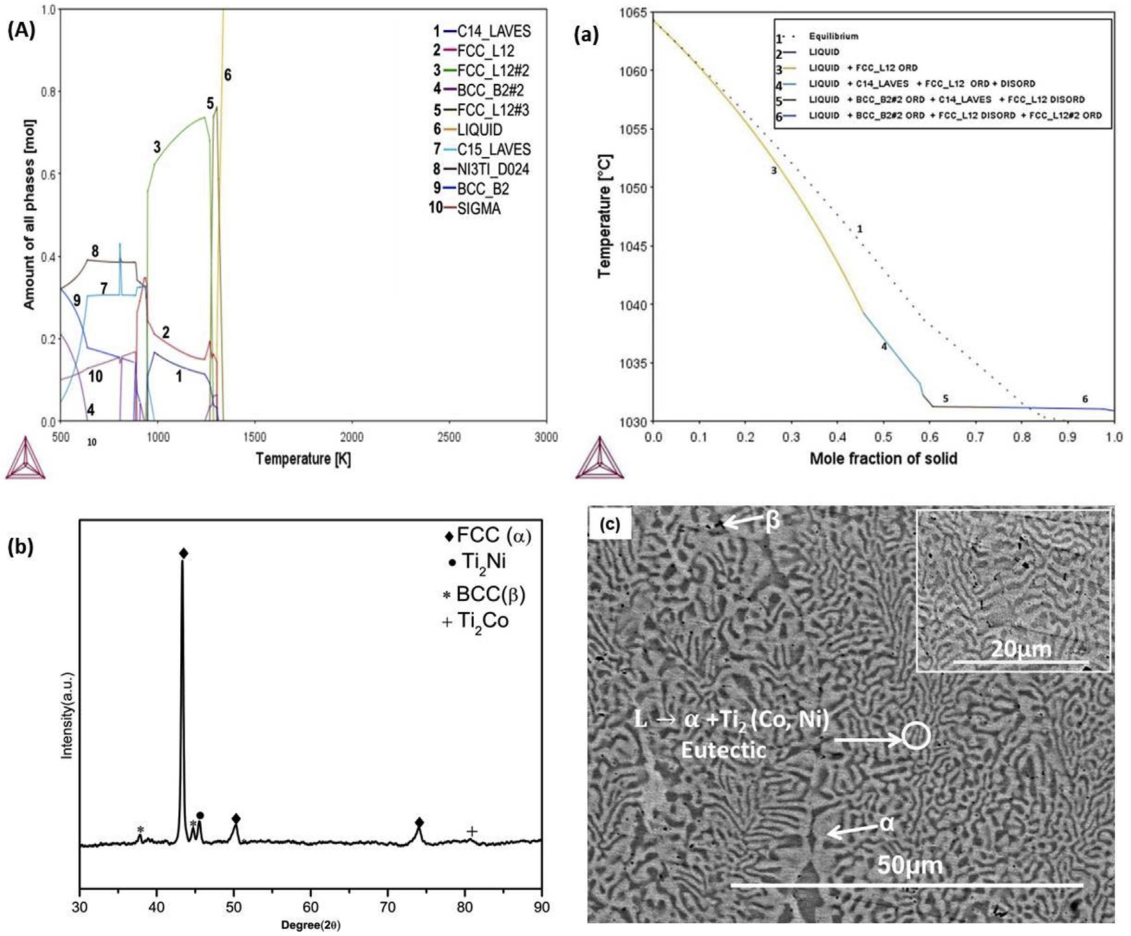

Fig. 1. **(A)** Amount of phases with temperature diagram, **(a)** Scheil's Solidification Pathway **(b)** XRD plot and **(c)** SEM micrograph of $Co_{25}Fe_{25}Mn_5Ni_{25}Ti_{20}$ EHEA.

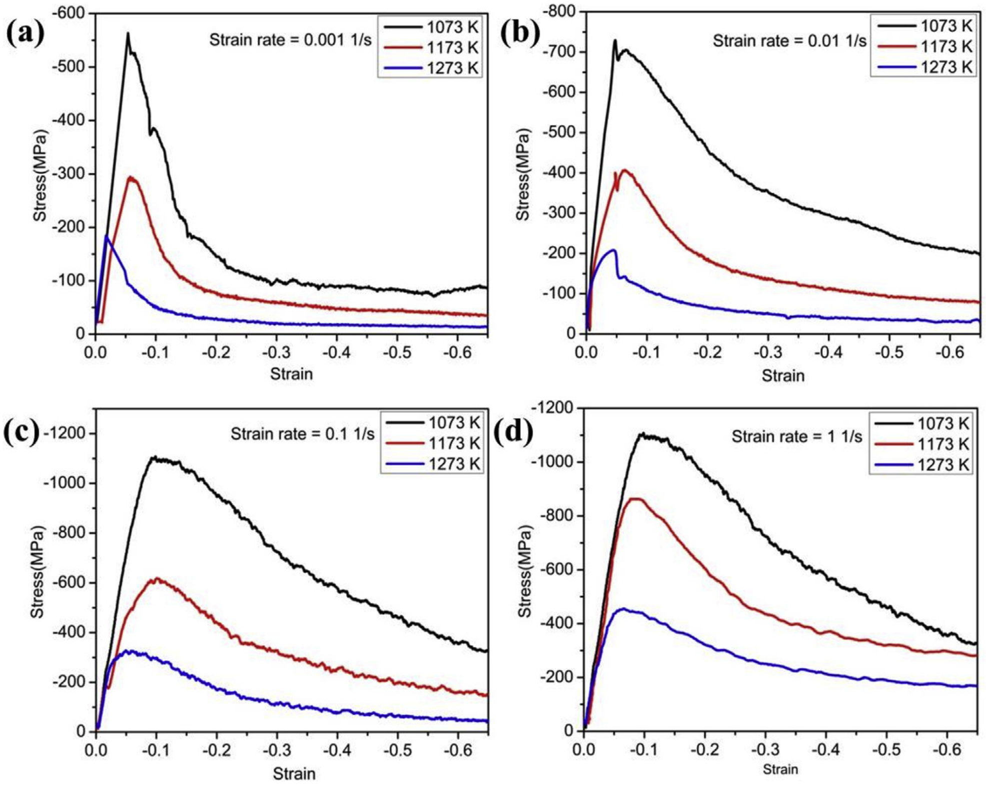

Fig. 2. True stress-strain plot for $Co_{25}Fe_{25}Mn_5Ni_{25}Ti_{20}$ EHEA at different temperature (K) and strain rate (s^{-1}), **(a)** 0.001, **(b)** 0.01, **(c)** 0.1. **(d)** 1.

stress is reached, the dislocation density increases multiplies significantly, and hence the flow stress increased rapidly with increase in strain at a particular temperature and attains the maximum. Furthermore, after peak stress, the softening process becomes dominant, and hence the stress falls with increase in strain at a fixed temperature [29–31].

3.2. *Constitutive equation and calculation of activation energy and materials constant*

The constitutive equation is the correlation of true stress, deformation temperature and strain rate. The stress-strain value obtained from the experimentally via a hot compression test can be used to calculate the activation energy and material constant. It is reported [32–34] that the simple power-law correlates the flow stress, deformation temperature and strain rate. It is important to note here that the activation energy gives the information about the deformation mechanism which is correlated with the microstructural evolution, mainly dislocation movement, dynamic recovery (DRV), dynamic recrystallisation (DRX) and grain boundary movement [14].

According to the constitutive equation, the activation energy is supposed to be a constant physical parameter which can be determined using power law:

$$\dot{\varepsilon} = A_1\ \sigma^n \exp\left[\frac{Q}{RT}\right] \tag{1}$$

After taking the logarithm of both sides and differentiating the equation. Finally, the activation energy is expressed as

$$Q = 2.303R\ \{(\partial \log \dot{\varepsilon})/(\partial \log \sigma)\}T\{\partial \log \sigma/\partial(1/T)\}\dot{\varepsilon} \tag{2}$$

Where, $\frac{\partial \log \dot{\varepsilon}}{\partial \log \sigma}$ is the slope of the log$\dot{\varepsilon}$ *Vs.* log σ and $\frac{\partial \log\sigma}{\partial\left(\frac{1}{T}\right)}$ is a slope of the logσ *Vs.* 1/T and R = universal gas constant (8.314 J mol $^{-1}$K).

The activation energy (Q) at a strain 0.65 for studied EHEA has been calculated by drawing a plot between log$\dot{\varepsilon}$ *Vs.* log σ at different temperature and between logσ vs 1/T at different strain rate which are given in Fig. 3(a) and (b), respectively. The typical value of activation energy (Q) for studied EHEA at strain 0.65 is found to be 311 kJ/mol, and stress exponent (n) value is 3.5. Further, the activation energy (Q) is estimated as 362 kJ/mol, 293 kJ/mol, 273 kJ/mol, 284 kJ/mol, 287 kJ/mol and 293 kJ/mol at true strain 0.1, 0.2, 0.3, 0.4, 0.5 and 0.6 respectively. Therefore, the constitutive equation at true stain 0.65 as a function of strain rate ($\dot{\varepsilon}$) and temperature (T) for studied EHEA can be described as follows:

$$\dot{\varepsilon} \sim \sigma^{3.5}\ \exp\left(\frac{311000}{RT}\right) \tag{3}$$

Though, it is essential to observe that this constitutive equation for studied EHEA defines the stress and strain rate relation in the temperature between 800 °C and 1050 °C. Rahul et al. [35] found that n and Q values are 5.6 and 306 kJ/mol, respectively for $AlCoCrFeNi_{2.1}$ EHEA in the deformation temperature range of 800°C–1100 °C. It is also reported for $Co_{20}Cu_{20}Fe_{20}Ni_{20}Ti_{20}$ EHEA [36] that n and Q values are obtained as 3.1 and 316 kJ/mol at strain 0.7, respectively. The calculated activation energy (Q ~ 311 kJ/mol) of investigated EHEA at the last stage of the hot deformation (i.e. at true strain 0.65) is comparable to the commercial Ti–6Al–4V alloys (i.e. Q ~265–370 kJ/mol) [37]. Usually, higher is the activation

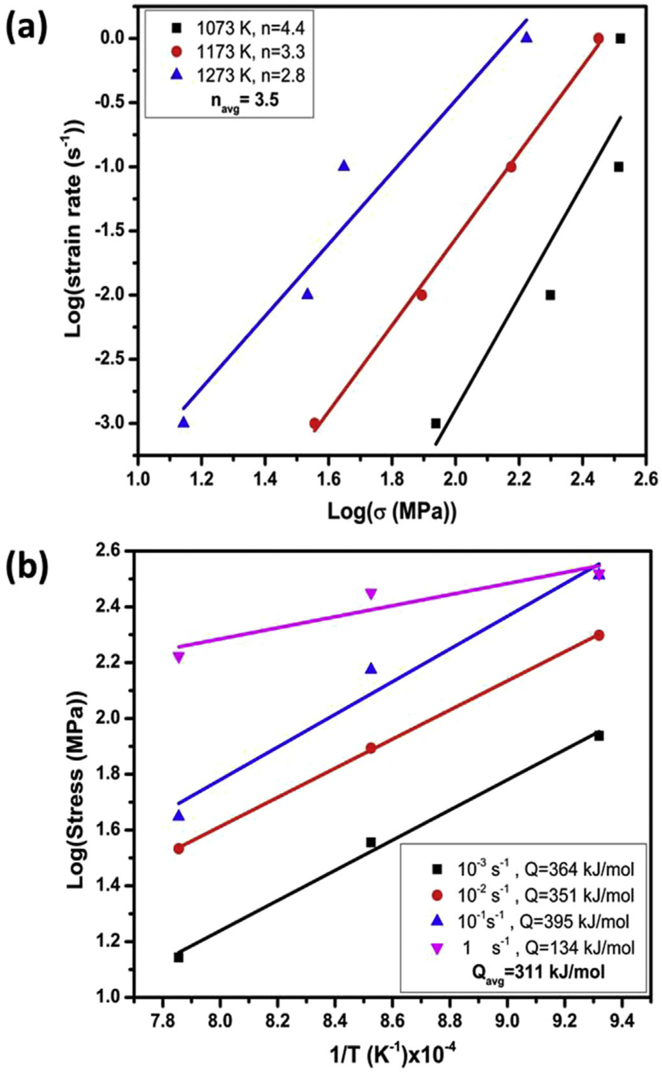

Fig. 3. Plot between (a) Log $\dot{\varepsilon}$ and Log σ (b) Log σ and 1/T; used for calculating the activation energy (Q) and stress exponent (n) at true strain 0.65.

energy, better the strength of material at elevated temperature. The calculated activation energy at a different stage of hot deformation is shown in the supplementary file as a Fig. 1(S). It is important to note that all alloying element in EHEAs consider as substitutional solutes, the activation energy for the interaction of the solute atoms with dislocation consist of a combination of both energies for the vacancy formation as well as energy for solute motion [36].

4. Deformation windows and processing maps

It is to be noted that the processing maps of studied EHEA are constructed based on the dynamic material modelling (DMM) and the combination of two contour maps, i.e. iso-efficiency (η) and instability factor $\xi\,\overline{(\dot{\varepsilon})}$. The energy absorbed (P) during the hot working process is defined as a multiplication of effective stress and strain rate. Prasad et al. [38] proposed that the total energy absorbed is divided into two fractions i.e. E_P and E_M, where E_P is the dissipation of energy during plastic deformation, and E_M is energy related to the microstructural changes during metallurgical processes. The overall energy absorbed can be expressed as:

$$P = \sigma\dot{\varepsilon} = \int_0^{\varepsilon} \sigma d\dot{\varepsilon} + \int_0^{\sigma} \dot{\varepsilon} d\sigma = E_P + E_M \tag{4}$$

Where σ is effective stress and $\dot{\varepsilon}$ is the strain rate. Two-parameters such as the dissipation efficiency (η) and the instability factor $\xi\,\overline{(\dot{\varepsilon})}$ are represented in that model. η is defined as the ratio of E_M and maximum possible E_M.

$$\eta = \frac{E_M}{E_M \max} = \frac{2m}{m+1} \tag{5}$$

Where m is the fundamental material properties, known as strain rate sensitivity factor.

The instability condition [38] is represented by dimensionless instability factor $\xi\,\overline{(\dot{\varepsilon})}$ as:

$$\xi\,\overline{(\dot{\varepsilon})} = \left[\partial \ln\left(\frac{m}{m+1}\right) \Big/ \partial ln\dot{\varepsilon}\right] + m < 0 \tag{6}$$

The iso-efficiency η and sensitivity factor related to strain rate (m) are the crucial parameters to define the stable and unstable conditions during hot deformation. Therefore, it has been reported [38] that the criteria for instability (i.e. 2 m < η ≤ 0) and stability (i.e. 0 < η ≤ 2 m) are valid for all stress-strain plots. Moreover, for stable plastic flow and homogenous flow of materials during deformation, the DMM model recommends followings criteria:

$$0 < m < 1 \tag{7}$$

$$\dot{m} < 0 \tag{8}$$

$$S \geq 1 \tag{9}$$

$$\dot{s} \leq 0 \tag{10}$$

Where σ = effective stress, T = Deformation temperature in K, $\dot{\varepsilon}$ is the strain rate, $\dot{m} = \frac{\delta m}{\delta log\dot{\varepsilon}}$ $s = \frac{\delta ln\sigma}{\delta\left(\frac{1}{T}\right)}$ and $\dot{s} = \frac{\delta s}{\delta log\dot{\varepsilon}}$

Here, m = Sensitivity factor related to strain rate,
$\dot{m}$ = Rate of change of sensitivity factor related to strain rate w.r.t. strain rate,
S= Sensitivity factor of effective stress related to temperature and
$\dot{s}$ = Rate of change of Sensitivity factor of effective stress related to temperature w.r.t. Strain rate

Fig. 4(a) shows the processing efficiency contour and instability maps for studied EHEA at strain at 0.65. The maximum efficiency shows the optimal processing conditions. However, the condition with peak efficiency may exhibit a negative instability parameter. It is found that the instability during the deformation occurs mainly due to cracks, localised plastic flow in the microstructure. It is reported [39] that different DMM stability factors are unable to predict the geometrical instability, i.e. excessive bulging during compression testing, necking during tensile testing and uneven deformation in axial and radial loading during torsion testing.

Moreover, a region of dense contour lines with high power dissipation efficiency and nearby unstable region are considered as metastable regions [40]. It is clear from Fig. 4(a) that higher value of efficiency (50–60%) is observed in the two domains. The first one lies in the temperature between 1073 K to 1200 K and strain rate between 10^{-3} s^{-1} to 10^{-2} s^{-1} and also in the temperature range

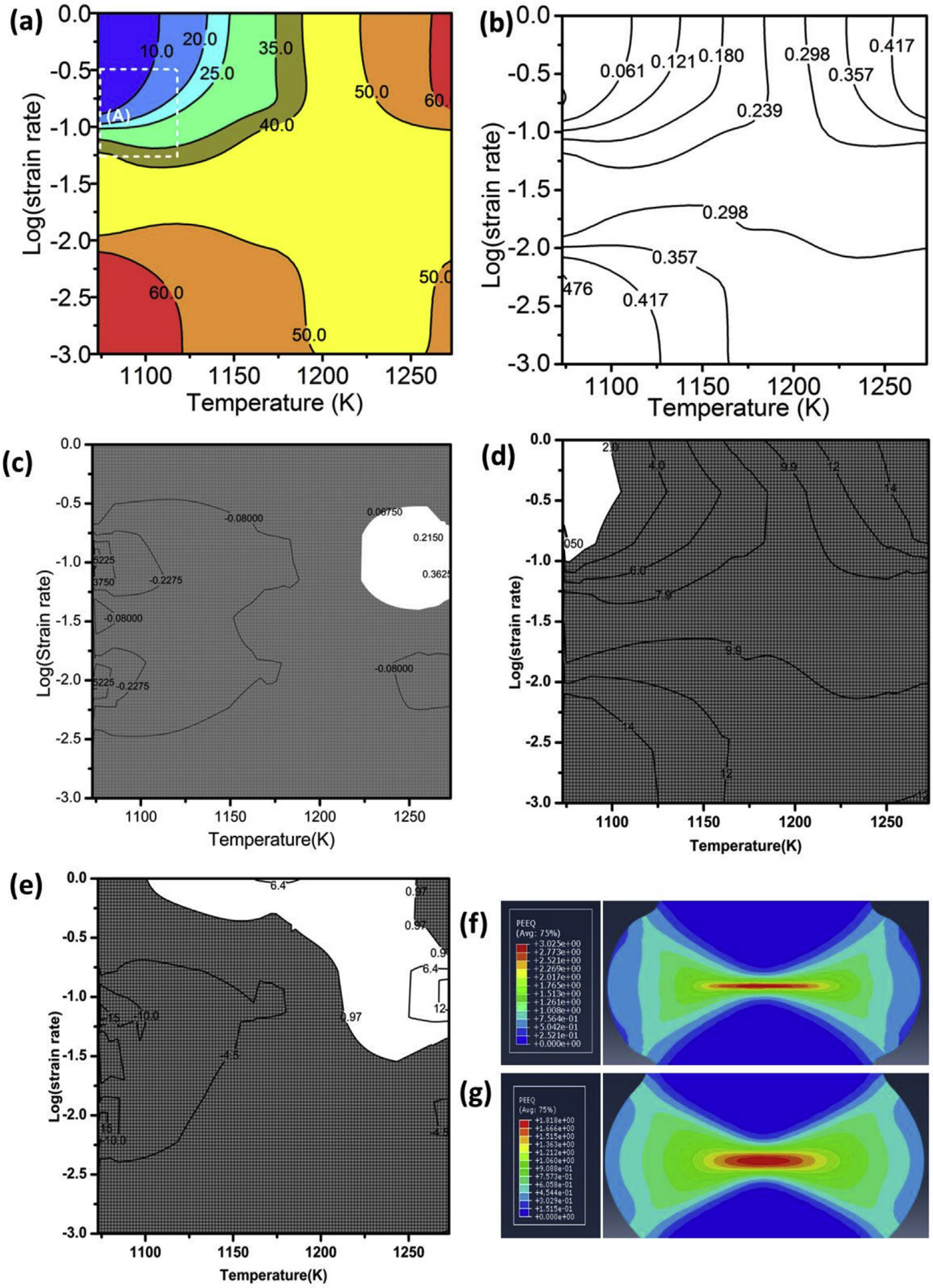

Fig. 4. Processing map at strain 0.65 (a) Efficiency of power dissipation (b) Strain rate sensitivity m (c) Rate of change of strain rate sensitivity w.r.t. strain rate $\dot{m}$ (d) s (e) $\dot{s}$and Simulated Effective plastic strain distribution at strain rate 1 and temperature (f) 1173 K (g) 1273K.

1225K–1273 K and strain rate 10^{-1} s^{-1} - 1 s^{-1}. As per the instability processing map, the processing instability factor $\xi \overline{(\dot{\varepsilon})}$ shows negative value at a temperature range between 1073 K to 1130 K and strain rate between $10^{-1.25}$ s^{-1} to $10^{-0.5}$ s^{-1}, which are presented by region A in Fig. 4(a). The sensitivity factor related to strain rate m (as shown in Fig. 4(b)) shows that the stability in all ranges of temperature and strain rate in processing maps. The stability regimes during hot deformation are also predicted by a parameter ($\dot{m}$) (hatched areas as shown in Fig. 4(c)) and also the stability region predicted by two other parameters s and $\dot{s}$ are indicated in Fig. 4(d) and (e) respectively as hatched areas. The prediction by parameter s and $\dot{s}$ shows the stable region in the temperature

Table 1
Microstructural features at different strain rate and Temperature.

	Strain rate range (s^{-1})	Temperature range (K)	Efficiency (η)	Microstructural features
Domain I: Stable regime	$10^{-1.55}$-$10^{-0.65}$,	1073–1200,	30–40,	Uniform distribution of phases,
	10^{-3}-$10^{-1.55}$,	1073–1273,	40–60,	Uniform distribution of phases,
	$10^{-1.40}$-$10^{-0.5}$	1073–1220	40–50	Uniform distribution of phases
Domain II: Unstable regime	10^{-1}-1,	1073–1105,	10–20,	Large cracks,
	$10^{-1.5}$-$10^{-0.4}$	1200–1273	40–50	Pores and Localised flow

ranges 1073K–1273K, 1105K–1273 K and strain rate ranges 10^{-3}-10^{-1} s^{-1}, 10^{-1}-1 s^{-1}. The workability regimes with different parameters of DMM model provided in the Supplementary file as Table 1S. Finally, DMM predicts the stable hot workability regimes in the temperature between 1073 K to 1273 K and strain rate between 10^{-3} s^{-1} to $10^{-1.55}$ s^{-1} as well as 1130 K–1225 K and strain rate $10^{-0.5}$ s^{-1} to 1 s^{-1}.

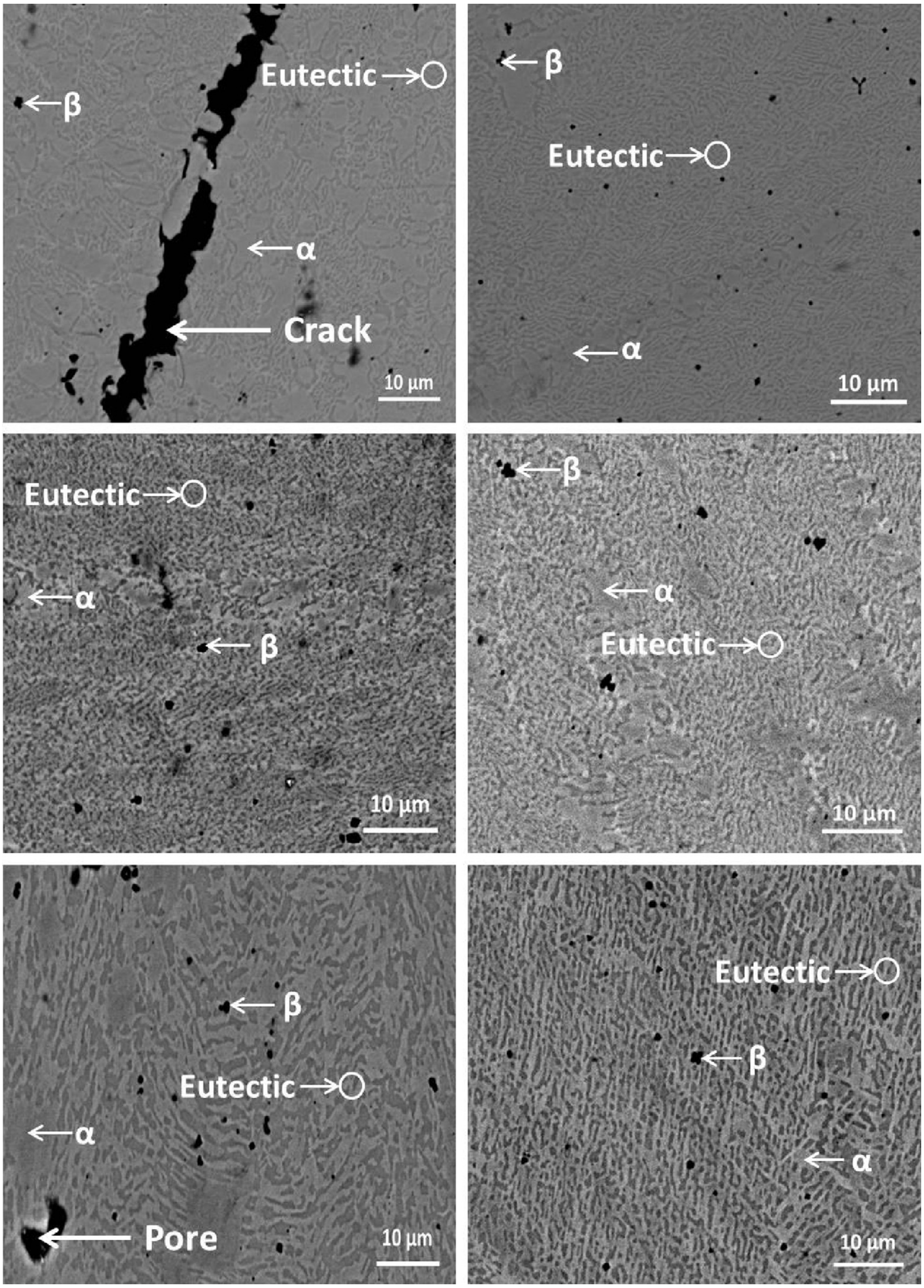

Fig. 5. SEM BSE images of hot deformed samples at (a) 800 °C@SR 1, (b) 800 °C@SR 0.1, (c) 800 °C@SR 0.01, (d) 900 °C@SR 0.1, (e) 1000 °C@SR 0.1 and (f) 1000 °C@SR 0.01.

5. FEM simulation

The FEM simulation can be used to identify the bulk deformation characteristics by identifying the strain, stress and strain rate fields in the material. By utilising this capability, the more sensitive zones in material flow regions with complex geometries can be identified in actual industrial production condition. The stress-strain flow curves obtained in Gleeble 3800® thermo-mechanical simulator at different sets of temperatures and strain rates were imported into ABAQUS ® FEM software to simulate the hot deformation behaviour. The constitutive equation can also be used for developing the material database. Effective plastic strain at a temperature of 1173 K and 1273 K and at strain rate 1 s^{-1} shown in Fig. 4(f) and (g). The strain field distribution confirms the inhomogeneous flow behaviour inside the material, resulting in the microstructural variation at different zones. The results obtained by simulation shows the higher value of effective plastic strain at the centre of the deformed sample for both temperatures and the maximum strain values depend on the temperature. It is important to note here that this inhomogeneity needs to take into consideration while characterizing material for high-temperature applications.

6. Microstructural analysis of deformed samples

The detailed microstructural characterization of the deformed EHEA at different hot working conditions was carried out to correlate with the observation drawn from the developed contour plots using various parameters. However, The representative SEM micrograph of deformed sample is shown in Fig. 5. It is found that the cracks are observed in the deformed specimen at temperature of 800 °C and strain rate of 1 s^{-1} (as shown in Fig. 5(a)) and this instability is matched with the region in the contour plot developed using the parameter s. In Fig. 5(b), (c), (d) and (f), it is found that a uniform distribution of phases as well as cracks and pores free microstructure at different temperatures and strain rates. It is to be noted that the contour plots generated using various parameters show a stable zone at 800 °C (strain rate = 0.01 s^{-1}), 900 °C (strain rate = 0.1 s^{-1}) as well as 1000 °C (strain rate = 0.01 s^{-1}), but the unstable zone is observed at 800 °C (strain rate = 0.1 s^{-1}). Further, the porosity is found in a deformed specimen at 1000 °C (strain rate = 0.1 s^{-1}) (shown in Fig. 5(e)), which corroborates with the instability regimes in the generated contour plots using parameters such as $\dot{m}$ and $\dot{s}$. It is evident in the stable regime that microstructural constituents are uniformly distributed throughout the whole specimen and elongated grains are observed in the direction perpendicular to the compression axis. While in the unstable regime, the localised plastic deformation, cracks and pores are observed in the microstructure of the deformed sample. It is important to note that the deformation temperature and strain rate play an essential role in the microstructural evolution of deformed EHEAs. The microstructural features at different strain rate (s^{-1}) and Temperature (K) are provided in Table 1. Therefore, uniform distribution of phases and crack free microstructure of EHEA are necessary for processing of materials at high-temperature and hence can be considered as potential candidate materials for high-temperature structural applications.

7. Conclusion

The hot deformation behaviour of the studied $Co_{25}Fe_{25}Mn_5Ni_{25}Ti_{20}$ EHEA was examined by conducting the compressive test in Gleeble thermo-mechanical simulator in the temperature between 1073 K to 1273 K and strain rate between 10^{-3} s^{-1} to 1 s^{-1}. Based on the above results and discussions, the following outcomes can be summarized for studied EHEA.

- The studied EHEA shows the peritectic reaction between bcc (β) and liquid phase (L) to form fcc (α) (i.e. bcc (β) + Lα fcc (α) as well as eutectic reaction between fcc (α) and Ti_2(Ni, Co) (i.e. (i.e. L→fcc (α)+Ti_2(Ni, Co)).
- The average activation energy (Q) for hot deformation of studied EHEA is 311 kJ/mol, and stress exponent n is 3.5. The constitutive relation for the investigated EHEA is described by the equation as $\dot{\varepsilon} \sim \sigma^{3.5} \exp\left(\frac{311000}{RT}\right)$.
- The optimal hot workability regimes are identified by generating contour plots using dynamic materials modelling, and the thermomechanical processing parameters lie in temperature range 1073–1273 K and strain rate range 10^{-3} - $10^{-1.6}$ s^{-1} as well as 1130–1225 K and strain rate $10^{-0.5}$-1 s^{-1}.
- FEM simulation is used to understand the effective plastic strain distribution during deformation of studied EHEA at different temperature and strain rate 1 s^{-1}.

Declaration of competing Interest

The authors declare that they have no known competing financial interests or personal relationships that could have appeared to influence the work reported in this paper.

CRediT authorship contribution statement

Reliance Jain: Investigation, Formal analysis, Software, Writing - original draft. **M R Rahul:** Investigation, Formal analysis, Writing - review & editing. **Sumanta Samal:** Investigation, Methodology, Resources, Conceptualization, Formal analysis, Writing - review & editing, Supervision, Validation, Funding acquisition. **Vinod Kumar:** Formal analysis, Writing - review & editing. **Gandham Phanikumar:** Resources, Formal analysis, Writing - review & editing, Funding acquisition.

Appendix A. Supplementary data

Supplementary data to this article can be found online at https://doi.org/10.1016/j.jallcom.2019.153609.

References

[1] J.W. Yeh, et al., Nanostructured high-entropy alloys with multiple principal elements: novel alloy design concepts and outcomes, Adv. Eng. Mater. 6 (5) (2004) 299–303.

[2] B. Cantor, I.T.H. Chang, P. Knight, A.J.B. Vincent, Microstructural development in equiatomic multicomponent alloys, Mater. Sci. Eng. A 375–377 (1–2) (2004) 213–218.

[3] C. Hsu, J. Yeh, S. Chen, T. Shun, Wear resistance and high-temperature compression strength of Fcc CuCoNiCrAl0.5Fe alloy with boron addition, Metall. Mater. Trans. A 35A (2004) 1465–1469.

[4] L. Jiang, et al., Effect of Mo and Ni elements on microstructure evolution and mechanical properties of the CoFeNixVMoy high entropy alloys, J. Alloy. Comp. 649 (2015) 585–590.

[5] O.N. Senkov, S.L. Semiatin, Microstructure and properties of a refractory high-entropy alloy after cold working, J. Alloy. Comp. 649 (2015) 1110–1123.

[6] N.D. Stepanov, N.Y. Yurchenko, D.V. Skibin, M.A. Tikhonovsky, G.A. Salishchev, Structure and mechanical properties of the AlCrxNbTiV (x= 0, 0.5, 1, 1.5) high entropy alloys, J. Alloy. Comp. 652 (2015) 266–280.

[7] S. Chatterjee, P.P. Bhattacharjee, S. Guo, N. Tsuji, Ultrafine-Grained $AlCoCrFeNi_{2.1}$ Eutectic High-Entropy Alloy, Mater. Res. Lett. 4 (2016) 174–179.

[8] S. Samal, K. Biswas, Novel high-strength NiCuCoTiTa alloy with plasticity, J. Nanoparticle Res. (15) (2013) 1.

[9] Y.F. Kao, T.J. Chen, S.K. Chen, J.W. Yeh, Microstructure and mechanical property of as-cast, -homogenized, and -deformed AlxCoCrFeNi ($0 \leq x \leq 2$) high-entropy alloys, J. Alloy. Comp. 488 (1) (2009) 57–64.

[10] N.N. Guo, et al., Microstructure and mechanical properties of refractory MoNbHfZrTi high-entropy alloy, Mater. Des. 81 (2015) 87–94.

[11] W.H. Liu, et al., Ductile CoCrFeNiMox high entropy alloys strengthened by hard intermetallic phases, Acta Mater. 116 (2016) 332–342.

[12] B. Gludovatz, A. Hohenwarter, D. Catoor, E.H. Chang, E.P. George, R.O. Ritchie, A fracture-resistant high-entropy alloy for cryogenic applications, Science 345 (6201) (2014) 1153–1158.

[13] A. Deschamps, Y. Bréchet, Influence of quench and heating rates on the ageing response of an Al–Zn–Mg–(Zr) alloy, Mater. Sci. Eng. A 251 (1–2) (2002) 200–207.

[14] D. Sang, R. Fu, Y. Li, The hot deformation activation energy of 7050 aluminum alloy under three different deformation modes, Metals 6 (3) (2016) 49.

[15] Q.L. Pan, B. Li, Y. Wang, Y.W. Zhang, Z.M. Yin, Characterization of hot deformation behavior of Ni-base superalloy Rene'41 using processing map, Mater. Sci. Eng. A 585 (2013) 371–378.

[16] F. Reyes-Calderón, I. Mejía, J.M. Cabrera, Hot deformation activation energy (QHW) of austenitic Fe-22Mn-1.5Al-1.5Si-0.4C TWIP steels microalloyed with Nb, V, and Ti, Mater. Sci. Eng. A 562 (2013) 46–52.

[17] M.R. Rahul, R. Jain, S. Jain, S. Samal, V. kumar, Phase evolution and mechanical behaviour of Co–Fe–Mn–Ni–Ti eutectic high entropy alloys, Trans. Indian Inst. Met. 71 (11) (2018) 2795.

[18] J.E. Saal, I.S. Berglund, J.T. Sebastian, P.K. Liaw, G.B. Olson, Equilibrium high entropy alloy phase stability from experiments and thermodynamic modeling, Scr. Mater. 146 (2018) 5–8.

[19] J.-P. Muggianu, M. Gambino, J. Pierre Bros, Enthalpies de formation des alliages liquides bismuth-étain-gallium à 723 k. Choix d'une représentation analytique des grandeurs d'excès intégrales et partielles de mélange, J. Chim. Phys. 72 (1975) 83–88.

[20] F. Kohler, To calculate the thermodynamic data of a ternary system from the associated binary systems, Mon. Journals Chem. Relat. parts other Sci. 91 (1960) 738–740.

[21] G. Toop, C. Somis, Some new ionic concepts of silicate slags, CanadianMetallurgical Quarterly 1 (2) (1962) 129–152.

[22] U.R. Kattner, The thermodynamic modeling of multicomponent phase equilibria, J. Occup. Med. 49 (1997) 14–19.

[23] B. Gorr, M. Azim, H. Christ, T. Mueller, D. Schliephake, M. Heilmaier, Phase Equilibria, Microstructure, and High Temperature Oxidation Resistance of Novel Refractory High-Entropy Alloys 624, Journal of Alloys and Compounds, 2015, pp. 270–278.

[24] C. Zhang, F. Zhang, S. Chen, W. Cao, Computational Thermodynamics Aided High-Entropy Alloy Design, JOM 64 (7) (2012) 839–845.

[25] Tazuddin, N.P. Gurao, K. Biswas, In the quest of single phase multi-component multiprincipal high entropy alloys, J. Alloy. Comp. 697 (2016) 434–442.

[26] J.A. Dantzig, M. Rappaz. Solidification EPFL Press,Lausanne, Taylor & Francis, 2009, pp. 345–427.

[27] S. Samal, K. Biswas, G. Phanikumar, Solidification Behavior in Newly Designed Ni-Rich Ni-Ti-Based Alloys, Metallurgical and Materials Transactions A 47 (2016) 6214–6223.

[28] G.E. Dieter, Mechanical Metallurgy, 646, McGraw-Hill, 1961, pp. 58–62.

[29] H.J. McQueen, N.D. Ryan, Constitutive analysis in hot working, Mater. Sci. Eng. A 322 (1–2) (2002) 43–63.

[30] S.F. Medina, C.A. Hernandez, General expression of the Zener-Hollomon parameter as a function of the chemical composition of low alloy and microalloyed steels, Acta Mater. 44 (1) (1996) 137–148.

[31] W. Kingkam, N. Li, H.X. Zhang, C.Z. Zhao, Hot deformation behavior of high strength low alloy steel by thermo mechanical simulator and finite element method, IOP Conf. Ser. Mater. Sci. Eng. 205 (1) (2017).

[32] C. Zener, J.H. Hollomon, Effect of Strain Rate Upon Plastic Flow of Steel, J. Appl. Phys. 15 (1) (1944) 22–32.

[33] L. Saravanan, T. Senthilvelan, Constitutive equation and microstructure evaluation of an extruded aluminum alloy, J. Mater. Res. Technol. 5 (1) (2016) 21–28.

[34] Y.C. Lin, M.S. Chen, J. Zhong, Effect of temperature and strain rate on the compressive deformation behavior of 42CrMo steel, J. Mater. Process. Technol. 205 (1–3) (2008) 308–315.

[35] M.R. Rahul, S. Samal, S. Venugopal, G. Phanikumar, Experimental and finite element simulation studies on hot deformation behaviour of AlCoCrFeNi2.1 eutectic high entropy alloy, J. Alloy. Comp. 749 (2018) 1115–1127.

[36] S. Samal, M.R. Rahul, R.S. Kottada, G. Phanikumar, Hot deformation behaviour and processing map of Co-Cu-Fe-Ni-Ti eutectic high entropy alloy, Mater. Sci. Eng. A 664 (2016) 227–235.

[37] S. Roy, S. Suwas, The influence of temperature and strain rate on the deformation response and microstructural evolution during hot compression of a titanium alloy Ti-6Al-4V-0.1B, J. Alloy. Comp. 548 (2013) 110–125.

[38] Y.V.R.K. Prasad, K.P. Rao, S. Sasidhara, Hot Working Guide A Compendium of Processing Maps, " *ASM Int.*, 2015, p. 636.

[39] S. Semiatin, V. Seetharaman, I. Weiss, Flow behavior and globularization kinetics during hot working of Ti–6Al–4V with a colony alpha microstructure, Mater. Sci. Eng. A 263 (2) (1999) 257–271.

[40] H. Wang, C. Wang, Y. Mo, H. Wang, J. Xu, Hot deformation and processing maps of Al-Zn-Mg-Cu alloy under coupling-stirring casting, J. Mater. Res. Technol. 8 (1) (2019) 1224–1234.